Check for updates

Thickness-dependent ultrafast charge-carrier dynamics and coherent acoustic phonon oscillations in mechanically exfoliated PdSe₂ flakes†

Chang-Fu Huo,[a] Rui Wen,[a] Xiao-Qing Yan, [ID]*[a] De-Kang Li,[a] Kai-Xuan Huang,[a] Yizhi Zhu,[b] Qiannan Cui,[b] Chunxiang Xu, [ID][b] Zhi-Bo Liu [ID]*[acd] and Jian-Guo Tian[acd]

Recently, palladium diselenide (PdSe₂) has emerged as a promising material with potential applications in electronic and optoelectronic devices due to its intriguing electronic and optical properties. The performance of the device is strongly dependent on the charge–carrier dynamics and the related hot phonon behavior. Here, we investigate the photoexcited–carrier dynamics and coherent acoustic phonon (CAP) oscillations in mechanically exfoliated PdSe₂ flakes with a thickness ranging from 10.6 nm to 54 nm using time-resolved non-degenerate pump–probe transient reflection (TR) spectroscopy. The results imply that the CAP frequency is thickness-dependent. Polarization-resolved transient reflection (PRTR) measurements reveal the isotropic charge–carrier relaxation dynamics and the CAP frequency in the 10.6 nm region. In addition, the deformation potential (DP) mechanism dominates the generation of the CAP. Moreover, a sound velocity of 6.78×10^3 m s^{-1} is extracted from the variation of the oscillation period with the flake thickness and the delay time of the acoustic echo. These results provide insight into the ultrafast optical coherent acoustic phonon and optoelectronic properties of PdSe₂ and may open new possibilities for PdSe₂ applications in THz-frequency mechanical resonators.

Introduction

Recently, two-dimensional (2D) materials have attracted significant attention due to their outstanding physical properties and potential applications in electronics and optoelectronics.[1–3] For example, black phosphorus (BP) has a wide thickness-tunable band gap,[4,5] a high carrier mobility,[6,7] and prominent anisotropy.[8] It has been applied in field-effect transistors (FETs) and gas sensors.[9,10] However, its poor air stability limits its broad practical applications.[11–15] As a new member of the 2D transition metal dichalcogenide (TMD) family, PdSe₂ has

demonstrated unique physical properties such as a high carrier mobility, a large on/off ratio,[16,17] a thickness-tunable phase transition (a semiconductor–semi-metal transition with increasing thickness),[18] superior ambipolar characteristics,[16] long-term air stability, and a linear dichroism transition.[19] Owing to its small band gap, few-layer PdSe₂ has been used to fabricate near-infrared to far-infrared photodetectors with high sensitivity and stability.[20,21]

PdSe₂ has also shown potential for optical and optoelectronic applications due to its thickness-tunable band gap, which can be narrowed from 1.3 eV for the monolayer to 0 eV in the bulk.[20] Recent optical measurements have revealed a phase transition from a semiconductor (monolayer) to a semi-metal (bulk).[18] A PdSe₂ transport layer has been applied in a semiconductor device and a thick layer (above 50 layers) was used in a semi-metallic device. The device based on PdSe₂ exhibited a strong polarization-dependent photoresponse,[22] adding additional degrees of freedom in the design and applications of the device. Photodetectors based on different thicknesses of PdSe₂ have shown a high photoresponsivity,[23] an ultra-broadband response[20] and the potential to be integrated with silicon photonics. Besides, it has been demonstrated that different thicknesses of PdSe₂ can be applied in other optoelectronic

[a] *The Key Laboratory of Weak Light Nonlinear Photonics, Ministry of Education, School of Physics and Teda Applied Physics Institute, Nankai University, Tianjin 300071, China. E-mail: yanxq01@nankai.edu.cn, liuzb@nankai.edu.cn*

[b] *State Key Laboratory of Bioelectronics, School of Biological Science and Medical Engineering, Southeast University, Nanjing 210096, China*

[c] *Renewable Energy Conversion and Storage Center, Nankai University, Tianjin 300071, China*

[d] *The collaborative Innovation Center of Extreme Optics, Shanxi University, Taiyuan, Shanxi 030006, China*

† Electronic supplementary information (ESI) available: AFM results, bandgap extraction, polarization-dependent Raman spectra, anisotropy in the Raman intensity, schematic diagram of experimental setup, the curves of the FFT, polarization dependence of normalized curves. See DOI: 10.1039/d1cp03202j

devices, including p-BP/n-PdSe$_2$ near-infrared photodiodes,[24,25] PdSe$_2$/SiNWA heterostructure-based photovoltaic detectors,[26] and Q-switched lasers based on PdSe$_2$ nanosheets.[27] The application of PdSe$_2$ in other types of device has also been investigated, such as in infrared imaging and humidity sensing.[26,28]

For these optoelectronic devices, photoexcited carrier dynamics and the photoresponse process of different thicknesses of PdSe$_2$ play a key role in optimizing the performance of the devices. Phonon vibrations are crucial in understanding heat dissipation and charge–carrier mobility in the device. Thus, studying the carrier dynamics and phonon vibrations in PdSe$_2$ is important.[29] However, a chemical vapor deposition (CVD) sample is prone to defects during the growth process. Defects have a great influence on the carrier-relaxation processes of 2D materials.[30,31] PdSe$_2$ exhibits distinct in-plane optical anisotropy due to its unique pentagonal structure. To reveal the anisotropy of the carrier-relaxation process of PdSe$_2$ satisfactorily, the measured sample should have a good crystal quality.
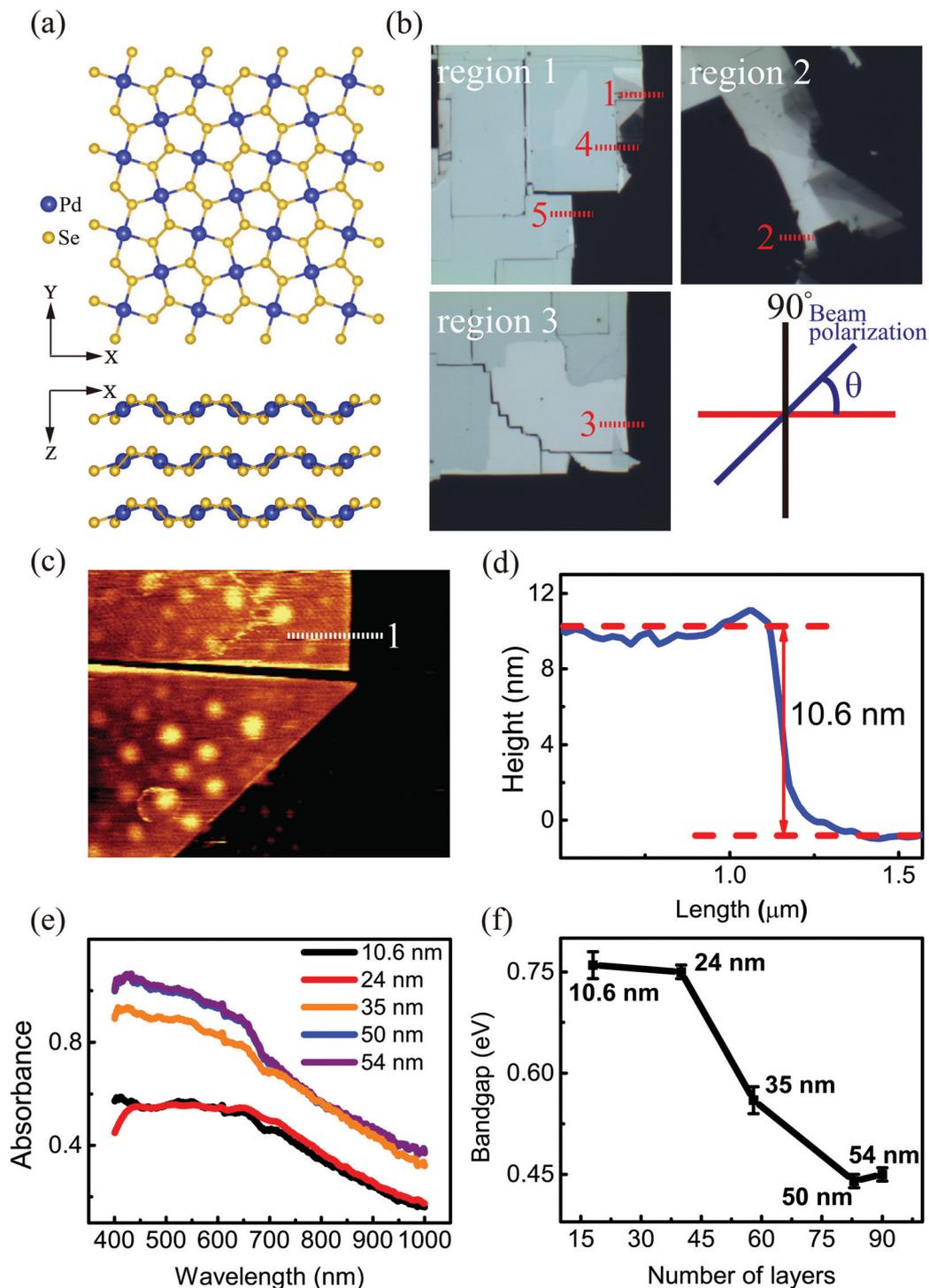
In this paper, we investigate the intrinsic photoexcited carrier dynamics and CAP oscillations of high-quality mechanically exfoliated PdSe$_2$ flakes with a thickness ranging from 10.6 nm to 54 nm using time-resolved non-degenerate pump–probe transient reflection (TR) spectroscopy. The results imply that the relaxation time and the CAP frequency are thickness-dependent. It was found that the fast recovery time is 12–53 ps and the slow relaxation time is 0.4–3.0 ns. The non-monotonic changes of the fast lifetime τ_1 and the slow lifetime τ_2 that dramatically decrease by an order of magnitude appear in the 35 nm region as the thickness is increased. This implies that the fast recovery times are attributed to carrier–carrier and carrier–photon scattering and that band gap narrowing causes the decrease of the slow decay times. Polarization-resolved transient reflection (PRTR) measurements reveal the isotropic charge–carrier relaxation dynamics and the CAP frequency in the 10.6 nm region. In addition, the deformation potential (DP) mechanism dominates the generation of the CAP. Moreover, a sound velocity of 6.78×10^3 m s^{-1} is extracted from the variation of the oscillation period with the flake thickness and the delay time of the acoustic echo.

Results and discussion

The top and side views of the pentagonal crystal structure of PdSe$_2$ are illustrated in Fig. 1(a).[17] The unit cell of bulk PdSe$_2$ is of the orthorhombic structure with the space group $Pbca$ (no. 61) and D_{2h} point group symmetry.[17,32] Each Pd atom is covalently bonded to four Se atoms.[33] PdSe$_2$ flakes, with different thicknesses, were isolated from the bulk PdSe$_2$ crystal using mechanical exfoliation. It is very difficult to obtain thin samples using mechanical exfoliation due to the strong interlayer coupling of PdSe$_2$.[34] Optical microscopy images (in reflection geometry) of the flakes exfoliated on fused quartz are shown in Fig. 1(b). The area uncovered by the PdSe$_2$ sample is black due to the use of a transparent substrate. Fig. 1(b)

shows the different thicknesses of three PdSe$_2$ regions. The three images in Fig. 1(b) are labeled as region 1, region 2 and region 3, respectively. The numbers 1–5 indicate the order of the different thicknesses. Next, the thickness of the different PdSe$_2$ regions was measured using atomic force microscopy (AFM). Fig. 1(c) shows the number 1 AFM data taken from PdSe$_2$ in region 1, which corresponds to the profile (red line) near the dashed red lines in Fig. 1(b) (for the other AFM results, see Fig. S1 in the ESI†). The AFM studies show that the thickness range of the flakes was from $\sim$10.6 nm to $\sim$54 nm. As previously reported, the thickness of the monolayer crystals was $\sim$0.6 nm.[17] The number of layers is from $\sim$18 to $\sim$90 layers. For simplicity, we will use D1, D4, D5 in region 1 (Fig. 1(b)), D2 in region 2 (Fig. 1(b)) and D3 in region 3 (Fig. 1(b)) to represent for the PdSe$_2$ flakes with different thicknesses from thin to thick in the following discussion. As shown in Fig. 1(e), optical absorption measurements were carried out to determine the thickness-dependent band gap. Fig. 1(e) shows a broadband absorption response with a smooth absorption band over a wide wavelength range from $\sim$400 to $\sim$1000 nm. The absorbance (Abs) was calculated as $\mathrm{Abs} = \log_{10} \dfrac{(I_0 - I_B) - (I_S - I_B)}{(I_0 - I_B)}$, where I_0 and I_S are the light intensities transmitted through the SiO$_2$ substrate and the PdSe$_2$ sample, respectively, and I_B is the background noise intensity of the instrument and the surrounding environment. We determine the absorption coefficient δ from the absorbance Abs as Abs $= \delta I$, where I is the incident light intensity and δ is the absorption coefficient. The photon energy $h\nu$ is the energy of the incident photons. Because PdSe$_2$ is an indirect band gap semiconductor, $\gamma = 2$ was adopted for $\delta h\nu \propto (h\nu - E_g)^\gamma$,[35] where E_g is the optical band gap. The optical band gap (see Fig. S2 in the ESI†) was then determined by extrapolating the linear region in the Tauc plot of $(\delta h\nu)^{1/2}$ versus $h\nu$. Fig. 1(f) shows the optical band gaps versus the number of PdSe$_2$ layers; overall, the band gap decreases as the thickness increases. Earlier DFT calculations have shown that the band gap changes slightly with thickness when the number of layers is larger than 16 (it is inferred that a band gap difference of 50 nm and 54 nm-thick PdSe$_2$ should be less than 0.05 eV).[17] The uncertainty in the optical band gaps is about $\pm$0.02 eV for our measuring system. Thus, it is hard to distinguish small changes in the optical band gap as the thickness varies from 50 nm to 54 nm. Therefore, the nearly unchanged band gaps for 50 nm and 54 nm is probably due to the small band gap variation between the two thicknesses and the limited band gap resolution of our measurement system. The variation trend of the band gap with thickness is consistent with earlier reports.[17,36] However, the band gap value of thick PdSe$_2$ is different from the reported value in ref. 17 and is in agreement with the value reported in ref. 36. The band gap difference between ours and the result in ref. 17 may be caused by the lower NA of the objective and noise in the optical absorption measurements in ref. 17.

To determine the crystal axis of these PdSe$_2$ flakes, we performed polarization-resolved Raman spectra measurements

This journal is © the Owner Societies 2021

Phys. Chem. Chem. Phys., 2021, **23**, 20666–20674 | **20667**

Fig. 1 Characterization of the PdSe₂ flakes. (a) Top and side views of the structure of the puckered PdSe$_2$ crystal. (b) Optical microscope images of exfoliated few-layer PdSe$_2$ flakes on fused quartz, and the numbers 1–5 indicate the order of different thicknesses. All scale bars are 10 μm. (c) Corresponding atomic force microscope (AFM) image corresponding to number 1 in the first image of (b) labeled as region 1. The other two images in (b) are labeled as region 2 and region 3. (d) Corresponding thickness of PdSe$_2$. (e) Absorption spectra of PdSe$_2$ flakes. (f) Thickness-dependent optical band gap extracted from the Tauc plots of $\sqrt{\alpha h \nu}$ vs. $h\nu$ for various numbers of PdSe$_2$ layers.

under a parallel configuration (i.e., $e_i \| e_s$, where e_i and e_s denote the linear polarization of the incident and scattered light, respectively). To do this, we rotated the polarizers in the incident and scattered light paths to change the angle

α between the crystallographic orientation and the linear polarization orientation of the incident and scattered light (the blue line shown in Fig. S4, ESI†). The Raman spectrum of 10.6 nm is depicted in Fig. 2. The other Raman spectra are shown in
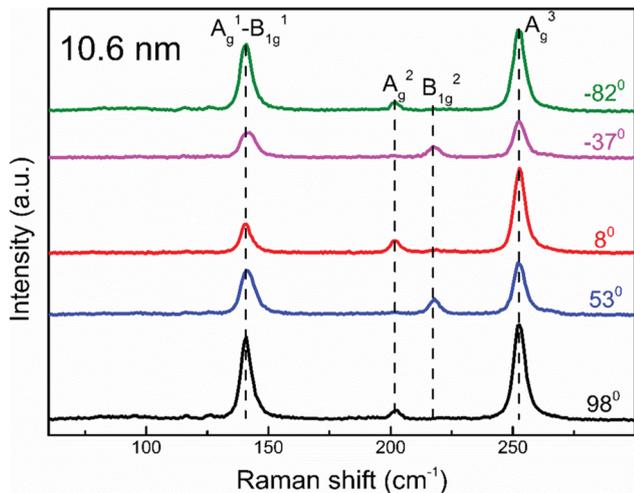
20668 | *Phys. Chem. Chem. Phys.*, 2021, **23**, 20666–20674

This journal is © the Owner Societies 2021

Fig. 2 Polarization-dependent Raman spectra of PdSe$_2$ with a thickness of 10.6 nm. Polarization orientations are shown in Fig. S4(d) (ESI†) – see red line (0°) and black line (90°). Raman spectra are shifted vertically for clarity.

Fig. S3 (ESI†). Four distinct Raman peaks were observed at the wavenumbers of ∼143, ∼206, ∼222, and ∼256 cm^{-1}, which correspond to the A$_g^1$–B$_{1g}^1$, A$_g^2$, B$_{1g}^2$, and A$_g^3$ modes, respectively, which are consistent with previous studies.[17,37] The A$_g^1$–B$_{1g}^1$, A$_g^2$, and B$_{1g}^2$ modes can be attributed to the movement of Se atoms, while the A$_g^3$ mode (at ∼256 cm^{-1}) represents the relative movement between the Pd and Se atoms. As expected, the Raman peak intensity is strongly dependent on the polarization of the excitation light due to its highly anisotropic optical response. A previous report has shown that the peak intensity of the A$_g$ (B$_{1g}$) mode oscillates with a periodicity of 180° (90°) as the orientation of the polarization is rotated.[37] Using the polar plot of the intensity of the A$_g^1$–B$_{1g}^1$ (∼143 cm^{-1}) mode (see Fig. S4 in the ESI†), it is inferred that the x axis is along the red line (0°), while the y axis is represented by the black line (90°) in Fig. 1(b). This offers a useful approach to determine the crystal orientation of the PdSe$_2$ flakes.

To investigate the evolution of the carrier and phonon dynamics with PdSe$_2$ thickness, time-resolved pump–probe TR measurements were performed using a home-built pump–probe system (see Fig. S5 in the ESI†). The TR measurements were carried out *via* pump excitation using a 520 nm fs pulse and probing with a 1040 nm fs pulse at room temperature. The pump-induced probe reflection change (ΔR) in the PdSe$_2$ flakes can be obtained by chopping the pump using an optical chopper and monitoring the output of the photodiode using a lock-in amplifier (Stanford Research Systems, SR865A). Fig. 3(a)–(e) shows the time-resolved ΔR traces of different PdSe$_2$ regions with a thickness ranging from ∼10.6 nm to ∼54 nm, respectively. The pump and probe beams were polarized along the 0° direction (parallel configuration). A clear negative differential reflection is observed around the zero delay time, which is followed by a rapid ΔR increase and a change to a positive value. Then, the positive differential reflection superimposed with a damped oscillation signal

decreases slowly to zero. $\Delta R < 0$ indicates photoinduced bleaching (PB), while $\Delta R > 0$ indicates photoinduced absorption (PA). The damped oscillation reflects the CAP dynamics during the process of charge-carrier recombination in these five regions.

To determine the relaxation times, we used a semi-log plot to fit the transient curves shown in Fig. 3 for reading the time constants. A tri-exponential decay function plus a damped exponentially attenuated oscillation term is used to fit the measured TR curves.[38–40]

$$y = A + B \exp\left(\frac{-t}{\tau_1}\right) + C \exp\left(\frac{-t}{\tau_2}\right) + D \exp\left(\frac{-t}{\tau_3}\right)$$
$$+ E \cos\left(2\pi\omega_p + \varphi\right)\exp\left(\frac{-t}{\tau_p}\right) \tag{1}$$

where A, B, C, D and E denote the fitting parameters, and t is the delay time between the pump and probe pulses. Furthermore, τ_1, τ_2 and τ_3 are the lifetimes of the three carrier-relaxation processes in few-layer PdSe$_2$. Here, we define $\tau_1 < \tau_2 < \tau_3$. The last exponentially decaying sinusoidal part was used to describe the CAP oscillation. E denotes the initial amplitude of the CAP oscillations, while ω_p and τ_p are the oscillation frequency and lifetime of the damped CAP oscillations, respectively. φ is the initial phase of the periodic oscillation. We combine the semi-log fit with the three-exponential fit for better evaluation of the time constants.

The extracted time constants τ_1, τ_2 and τ_3 for different thicknesses are shown in Fig. 3(f) and (g). It is shown that for the 10.6 nm thick region, the relaxation time of the PB signal consists of a fast lifetime τ_1 of ∼12 ps, τ_2 of ∼3 ns and τ_3 of ∼5 ns. For the 24 nm thick region, the relaxation time of the PB signal consists of a fast lifetime τ_1 which is increased to ∼29 ps. A non-monotonic change of the fast lifetime τ_1 appears for the 35 nm thick region. For the 35 nm, 50 nm and 54 nm thick regions, the fast relaxation time τ_1 of the PB signal is 41–53 ps. As the thickness increases (L = 24–54 nm), the slow decay time τ_2 decreases sharply and falls in the time range of 0.4–0.6 ns. The regions with thicknesses of 50 and 54 nm show similar relaxation times. The fast recovery time τ_1 of the PB signal is ∼46 ps for the 50 nm region. It is very close to the time constant of the 54 nm region ($\tau_1 \approx 41$ ps). The slow decay time for the 50 nm region ($\tau_2 \approx 0.6$ ns) is also close to that of the 54 nm region ($\tau_2 \approx 0.5$ ns). For the 10.6 nm, 24 nm, 35 nm and 50 nm regions, the slow recovery time τ_3 increases from ∼5 ns to ∼18 ns. The slow recovery time of the 50 nm region ($\tau_3 \approx 18$ ns) is larger than that of the 54 nm region ($\tau_3 \approx 10$ ns).

The TR curves shown in Fig. 3 indicate that PB around t = 0 s appears for 10.6 nm, 24 nm, 35 nm, 50 nm and 54 nm thick samples of region 1, region 2 and region 3. Furthermore, the increasing time of the signal indicates that thermalization and energy relaxation of hot carriers occurs on a ps time scale in this material. We attributed this fast time constant (τ_1) to carrier–carrier and carrier–phonon scattering during the carrier-cooling process. Carrier–phonon scattering causes lattice heating, which sets up a transient stress.[41] The TR curves also show that stress-wave-inducing coherent phonon
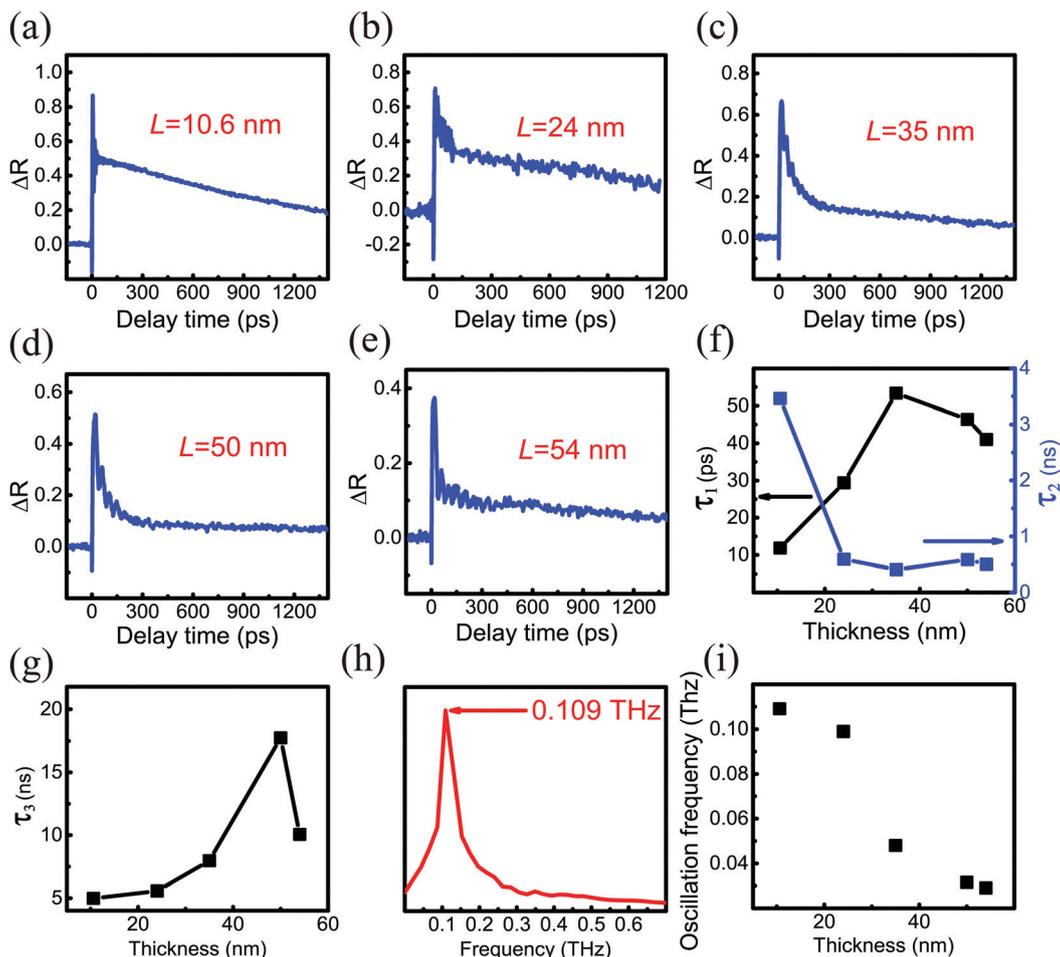
Fig. 3 (a–e) Time-resolved TR traces in different PdSe$_2$ regions. The pump (520 nm) and probe (1040 nm) beam fluences were 8 and 4.8 µJ cm^{-2}, respectively. (f and g) Variation of the time constant with the thickness. (h) Fast Fourier transform (FFT) of the oscillations from the TR traces of 10.6 nm. (i) Oscillation frequency *vs.* PdSe$_2$ thickness.

oscillation influences the process of hot carrier cooling. Then, the fast time constant (τ_1) of different thicknesses (L = 10.6–54 nm) is of the order of a few dozen picoseconds. The time-resolved ΔR traces of the five thicknesses show that the positive signal returned to equilibrium very slowly. The decay time τ_2 for the 10.6 nm think sample was about 3 ns, which is attributed to the interband relaxation time in semiconductors. However, for the 24 nm, 35 nm, 50 nm and 54 nm thicknesses, τ_2 decreases dramatically by an order of magnitude to 0.4–0.5 ns. As shown in Fig. 1(f), the band gap indicates a rapid decreasing trend from 24 nm to 50 nm. The band gaps of 50 nm and 54 nm are similar. The slow lifetime τ_2 values of 50 nm and 54 nm are very close. It is inferred that the band gap decrease with increasing PdSe$_2$ thickness causes a sharp decrease of the slow decay time τ_2 from 10.6 nm (18 layers) to 24 nm (40 layers). Therefore, it is reasonable to deduce that the sudden decrease of the relaxation time indicates the acceleration of the slow interband relaxation process due to band gap narrowing. When the thickness of PdSe$_2$ is larger than 50 layers (30 nm), PdSe$_2$ can be seen as a semi-metal.[17,18] For 35 nm, 50 nm and 54 nm, τ_2 is nearly thickness-independent. However,

the τ_2 of PtSe$_2$, which is an analogue of PdSe$_2$, is thickness-dependent.[42] The slow lifetime τ_3 is attributed to lattice cooling by dissipating the energy to the substrate.[43] Fig. 3(h) shows the fast Fourier transform (FFT) of the oscillations from the TR traces of the 10.6 nm thick sample (see Fig. S6 for more in ESI†). Fig. 3(i) indicates that the oscillation frequency decreases from 0.109 THz to 29 GHz with the increase of the thickness.

Because PdSe$_2$ exhibits distinct in-plane optical anisotropy due to its unique pentagonal structure, the polarization-resolved measurement of the TR curves in PdSe$_2$ is insightful. For the PdSe$_2$ flake in Fig. 1(b), the TR traces were measured at the D1 region (L = 10.6 nm). This was performed for a series of beam polarization angles θ, ranging from 0° (x axis) to 90° (y axis). The polarization angles of the pump and probe pulses were controlled by rotating half-wave plates and ensuring that they were parallel to each other, as in ref. 44. In this way, we could obtain the carrier dynamics of the PdSe$_2$ flake from the x axis to the y axis. As shown in Fig. 4(a), the negative signals of different angles are almost the same and the maximum values of the positive signals (anti-saturation absorption) increase from 0° to 90°. When the laser polarization approached the
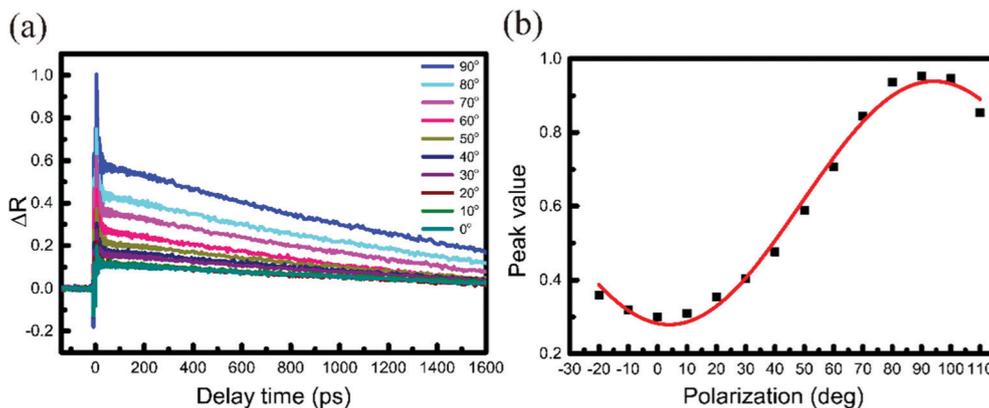
20670 | *Phys. Chem. Chem. Phys.*, 2021, **23**, 20666–20674

This journal is © the Owner Societies 2021

Fig. 4 (a) TR traces, recorded for a series of beam polarizations ranging from 0° to 90°, where the pump and probe polarization directions were parallel to each other. The beam polarization angle is shown in Fig. 1(b). The pump (520 nm) and probe (1040 nm) beam fluences were 8 and 4.8 μJ cm^{-2}, respectively. (b) Peak differential reflection signal as a function of beam polarization angles with respect to sample orientation.

90° direction, the positive signal is maximized, while its normalized decay time indicated no clear change (see Fig. S7 in the ESI†). The respective peak following a sinusoidal dependence on the polarization angle is shown in Fig. 4(b). This can be attributed to pump anisotropic absorption.[45]

As shown in Fig. 3(a)–(e), CAP oscillations appear in all these measured regions. The amplitude of the oscillation gradually decreases on a long time-scale, which can be attributed to three factors.[46–48] One is the process of a pump-induced stress wave, which spreads from the surface to the inner PdSe$_2$, where the absorption of each layer dampens the oscillation. The second factor is that the CAP energy of gradually weakens. The third factor is that the energy of the PdSe$_2$ lattice is gradually dissipated to the substrate and the surrounding environment. The oscillation frequencies were obtained using FFT of the time-resolved traces. Fig. 5(a) shows that the oscillation frequency has no obvious drift with changing laser polarization. This result implies that the oscillation frequency is independent of the pump–probe polarization (parallel configuration). Furthermore, Fig. 5(b) shows that the oscillation period has a linear dependence on the PdSe$_2$ thickness. As shown in Fig. 4(a) and 5(a), although PdSe$_2$ shows different light absorption under different polarizations, the oscillation frequency is independent of the polarization.

The observed oscillating signal should originate from the CAP oscillation, which could induce the reflection change of the time delayed probe *via* two forms including the photoelastic effect (the dielectric function being modified due to the presence of acoustic strain field, the first term in eqn (2)) and the interferometric effect (CAPs are able to displace surfaces and interfaces, the second term in eqn (2)). For a semi-infinite medium ($z = [0, +\infty]$), the transient differential reflectivity of the probe is written as follows:

$$\Delta R/R \propto \mathrm{Real}\left(\frac{4ik_0n}{1-n^2}\frac{\partial n}{\partial \eta}\int_0^\infty \eta(z,t)\mathrm{e}^{2ink_0z}\mathrm{d}z - 2ik_0u(0)\right) \quad (2)$$

where k_0, $u(0)$, n, $\eta(z,t)$ and $\frac{\partial n}{\partial \eta}$ are the probe light wave vector in a vacuum, the free surface displacement of the sample, the

complex optical index, stress and the photoelastic coefficient, respectively.[49] According to the signal being linearly dependent on the thickness, this can be attributed to the CAP standing wave. CAP oscillations have previously been studied in GaAs,[50] MoS$_2$,[41] PtSe$_2$,[46] BP,[44] and 2H-MoSe$_2$.[51] Coherent phonons are phonons that have the same phase when the crystal lattice vibrates. Phonons are divided into acoustic phonons and optical phonons. The acoustic phonon does a centroid motion, that is, each atom in the same unit cell does an overall motion. The optical phonon is a motion with the center of mass unchanged, that is, the relative vibration of different atoms in the unit cell. The acoustic mode can be regarded as a continuous medium elastic wave at low frequency. As previously reported, the pump-induced stress wave interferes with the reflected stress wave in the flakes to form a standing wave.[41] One surface of the film is free, but the other is in contact with the hard fused silica. Based on the standing-wave model, the oscillation period (T) can be described *via* the following formula under an approximately zero-displacement boundary condition:[52]

$$T = \frac{4d}{v} \quad (3)$$

where d is the thickness of PdSe$_2$ and ν is the sound velocity of the CAP. Based on this formula, we can calculate the sound velocity (6.78×10^3 m s^{-1}) from the slope of the linear fitting to the data in Fig. 5(b). The sound velocity (6.78×10^3 m s^{-1}) is close to the sound velocity of PtSe$_2$ (6.61×10^3 m s^{-1}).[53] The characteristics of the oscillation period are only dominated by the thickness, which is consistent with the fact that the oscillation period is independent of the pump–probe polarization.

Now, we focus on the generation mechanism of the CAP in our experiment. Two mainstream mechanisms can induce CAP oscillations: the DP and thermoelasticity (TE) mechanisms. For the DP mechanism, the action of light can modify the energy of the electronic distribution in the solid. Since the interatomic forces are indeed completely dependent on the electronic

This journal is © the Owner Societies 2021

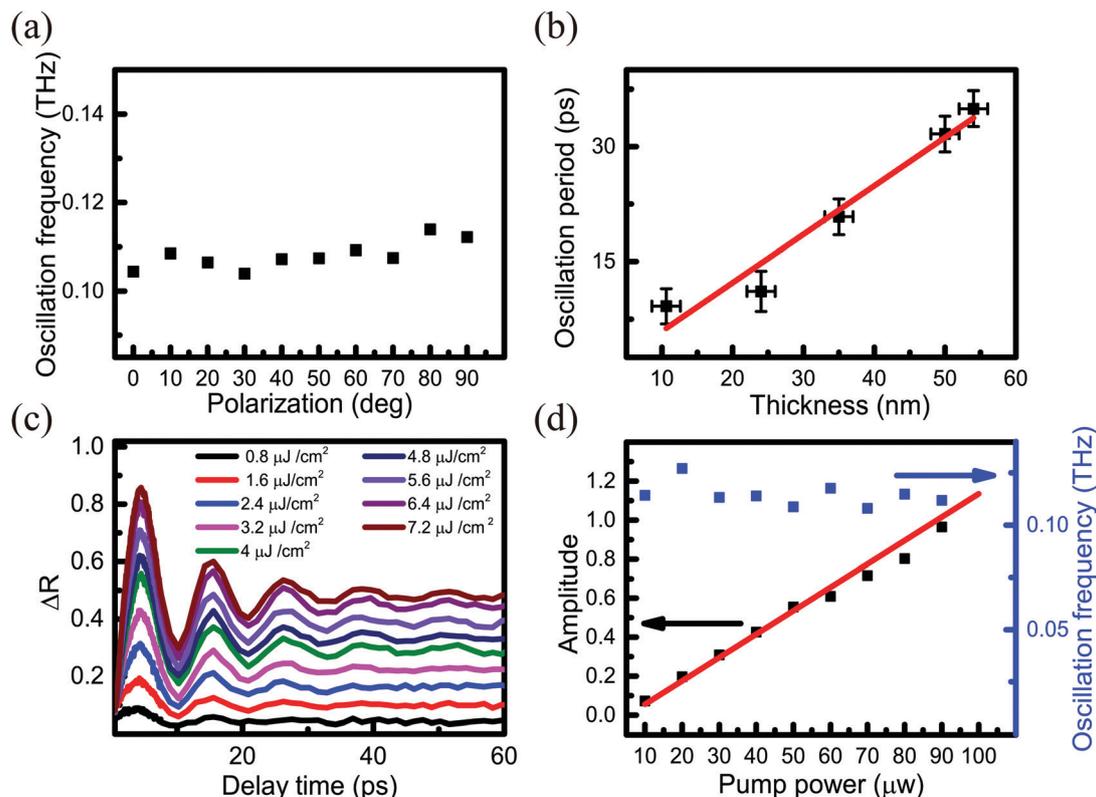*Phys. Chem. Chem. Phys.*, 2021, **23**, 20666–20674 | **20671**

Fig. 5   (a) Oscillation frequency as a function of the polarization angle. The oscillation frequency was obtained using the FFT of the TR traces in Fig. 4(a). (b) The oscillation period as a function of the PdSe$_2$ thickness follows a linear fit. (c) CAP oscillation for the 10.6 nm thick sample with different pump fluences. The probe fluence was 4.8 μJ cm^{-2}. (d) Initial amplitude of the coherent acoustic phonon oscillation as a function of the pump power shown in (a). The black dots represent the experimental data, and the red solid line is the linear fit. The right axis is the oscillation frequency for different pump fluences using the FFT. The blue dots represent the experimental data.

distribution, the action of light can further induce a modification of the interatomic forces *via* a change of the interactions between cations and electrons, cations and cations and electrons and electrons. Modification of the interatomic forces will result in a variation in the equilibrium position (*i.e.*, deformation occurs) of the lattice and the emission of acoustic phonons. The second mechanism of TE is related to lattice heating and elasticity. Under the action of light, the electrons are excited. The energy of the initially excited electrons is transferred to the phonon sublattice while the non-equilibrium carriers relax to lower energy levels *via* carrier–phonon scattering, then the lattice is heated. When relaxation processes take place, acoustic phonons are emitted and there is no definite phase relation for these emitted phonons.[49]

To investigate which mechanism is dominant in our experiment, we performed pump fluence-dependent measurements for the 10.6 nm thick flake. As shown in Fig. 5(c), similar temporal features in TR traces were observed for different pump fluences. Clearly, the amplitude of the CAP oscillations increased gradually with increasing pump fluence. The initial amplitudes of the CAP oscillations were extracted and are shown in Fig. 5(d). Based on the experimental results, it is inferred that the DP mechanism makes the dominating contribution due to the following three reasons:

(1) The measured PdSe$_2$ samples are a semiconductor material and with band gaps larger than 0.44 eV, and the extracted oscillation frequencies range from 29 GHz to 0.109 THz. In solids with a forbidden band, once the electrons in the valence band have been excited by light to the conduction band, the DP mechanism is usually important for roughly 1 GHz to 1 THz frequencies.[49]

(2) The DP mechanism is efficient for solids in which the lifetime of the photoexcited carriers is longer than the inverse of the CAP cyclic frequency.[49] The measured photoexcited carrier lifetime of PdSe$_2$ (larger than 5 ns) is longer than the period of the CAP (smaller than 35 ps). The photoexcited carrier lifetimes of PdSe$_2$ are longer than the period of the CAP oscillations.

(3) As previous reports have shown that the DP-generated CAP oscillation has a typical feature, the initial oscillation amplitude of the coherent acoustic phonon oscillation is proportional to the pump intensity at a relatively low power or fluence.[41,44] The measured initial amplitudes of the CAP oscillations of PdSe$_2$ are linearly correlated with the pump power/fluence and the oscillation frequency is independent of the pump power (Fig. 5(d)).

Therefore, the DP mechanism should dominate the CAP generation, and the TE mechanism contributes at longer delay

times. In addition, the linear dependence of the initial amplitude *vs.* the pump power allows us to rule out any significant role played by non-linear two-photon absorption in the transient reflection.

Summary

In summary, the photoexcited carrier dynamics and the CAPs of mechanically exfoliated PdSe$_2$ with different thicknesses were studied *via* time-resolved pump–probe differential reflection spectroscopy. The carrier dynamics of different thicknesses were investigated using time-resolved pump–probe TR spectroscopy. Polarization-resolved measurement of the TR in PdSe$_2$ reveals the isotropic charge–carrier relaxation dynamics and the CAP frequency in 10.6 nm region. Moreover, the DP mechanism dominates the CAP generation. A sound velocity of 6.78 × 10^3 m s^{-1} was determined based on the oscillation period of the CAP. These new phenomena in thin flakes have many potential applications in optical and THz resonator devices.

Experimental section

Sample fabrication and characterization

PdSe$_2$ flakes were fabricated *via* mechanical exfoliation from the bulk PdSe$_2$ crystal and transferred onto a fused silica substrate (2 mm thickness) using a stock tape. The thickness of the single PdSe$_2$ layer was ∼0.6 nm. The thicknesses of the samples (from 10.6 nm to 54 nm) were measured using atomic force microscopy (Witec Alpha 300) in tapping mode, with 0.1 nm vertical resolution and 8 nm resolution in the transverse direction. Raman spectra were measured with 532 nm laser excitation using the Witec Alpha 300 instrument. The light of the absorption spectra is a halogen lamp. The transmitted light was captured using a microscope objective (100× NA = 0.9) and directed using a spectrometer (PG 2000, Ideaoptics) equipped with a CCD camera (Exmor CMOS Sensor, Sony).

Transient reflection measurements

A Yb fiber-based laser (Menlo Systems) was used to provide ultrashort pulses with a central wavelength of 1040 nm and a 100 MHz repetition rate. The pulse width is ∼150 fs. The majority of the output is used as the probe beam and the minority is separated to generate at 520 nm pulse and used as the pump pulse. The probe fluence is attenuated *via* a combination of a half-wave plate and a Glan Taylor prism. Both the pump pulse and probe pulse were focused into the sample surface with a Gaussian spot, using an objective lens (Tu Plan Fluor 50× NA = 0.8, Nikon). Using this two-color pump–probe setup, the reflected pump beam was stopped from reaching the silicon photodetector using color filters. This significantly improved the signal-to-noise ratio. The reflection change (ΔR) of the probe beam due to the pump excitation was measured using a lock-in amplifier (SR865A, Stanford Research Systems) referenced to 1.5 kHz mechanically chopped pump (SR542, Stanford Research Systems).

Author contributions

Z.-B. L., X.-Q. Y. and C.-F. H. conceived the research. C.-F. H. performed the experiments and data analysis. Y.-Z. Z., Q.-N. C., and C.-X. X. measured the absorption spectra. C.-F. H., R. W., X.-Q. Y., D.-K. L., K.-X. H. and Z.-B. L. performed the theoretical analysis. C.-F. H., X.-Q. Y. and Z.-B. L. wrote the manuscript, which all authors read and commented on. Z.-B. L. and J.-G. T. supervised the project.

Conflicts of interest

The authors declare no competing financial interest.

Acknowledgements

References

1 Q. H. Wang, K. Kalantar-Zadeh, A. Kis, J. N. Coleman and M. S. Strano, *Nat. Nanotechnol.*, 2012, **7**, 699–712.

2 Y. Chen and M. Sun, *Nanoscale*, 2021, **13**, 5594–5619.

3 J. Fan, J. Song, Y. Cheng and M. Sun, *Results Phys.*, 2021, **24**, 104110.

4 V. Tran, R. Soklaski, Y. Liang and L. Yang, *Phys. Rev. B: Condens. Matter Mater. Phys.*, 2014, **89**, 235319.

5 P. Zereshki, Y. Wei, F. Ceballos, M. Z. Bellus, S. D. Lane, S. Pan, R. Long and H. Zhao, *Nanoscale*, 2018, **10**, 11307–11313.

6 H. Liu, A. T. Neal, Z. Zhu, Z. Luo, X. Xu, D. Tománek and P. D. Ye, *ACS Nano*, 2014, **8**, 4033–4041.

7 S. S. Lo, M. S. Devadas, T. A. Major and G. V. Hartland, *Analyst*, 2013, **138**, 25–31.

8 J. Qiao, X. Kong, Z.-X. Hu, F. Yang and W. Ji, *Nat. Commun.*, 2014, **5**, 1–7.

9 L. Li, Y. Yu, G. J. Ye, Q. Ge, X. Ou, H. Wu, D. Feng, X. H. Chen and Y. Zhang, *Nat. Nanotechnol.*, 2014, **9**, 372.

10 A. N. Abbas, B. Liu, L. Chen, Y. Ma, S. Cong, N. Aroonyadet, M. Köpf, T. Nilges and C. Zhou, *ACS Nano*, 2015, **9**, 5618–5624.

11 J. O. Island, G. A. Steele, H. S. van der Zant and A. Castellanos-Gomez, *2D Mater.*, 2015, **2**, 011002.

12 S. P. Koenig, R. A. Doganov, H. Schmidt, A. Castro Neto and B. Özyilmaz, *Appl. Phys. Lett.*, 2014, **104**, 103106.

13 J. D. Wood, S. A. Wells, D. Jariwala, K.-S. Chen, E. Cho, V. K. Sangwan, X. Liu, L. J. Lauhon, T. J. Marks and M. C. Hersam, *Nano Lett.*, 2014, **14**, 6964–6970.

This journal is © the Owner Societies 2021

Phys. Chem. Chem. Phys., 2021, **23**, 20666–20674 | **20673**

14 A. Castellanos-Gomez, L. Vicarelli, E. Prada, J. O. Island, K. Narasimha-Acharya, S. I. Blanter, D. J. Groenendijk, M. Buscema, G. A. Steele and J. Alvarez, *2D Mater.*, 2014, **1**, 025001.

15 A. Favron, E. Gaufres, F. Fossard, A. L. Phaneuf-L'Heureux, N. Y. Tang, P. L. Levesque, A. Loiseau, R. Leonelli, S. Francoeur and R. Martel, *Nat. Mater.*, 2015, **14**, 826–832.

16 W. L. Chow, P. Yu, F. Liu, J. Hong, X. Wang, Q. Zeng, C. H. Hsu, C. Zhu, J. Zhou and X. Wang, *Adv. Mater.*, 2017, **29**, 1602969.

17 A. D. Oyedele, S. Yang, L. Liang, A. A. Puretzky, K. Wang, J. Zhang, P. Yu, P. R. Pudasaini, A. W. Ghosh, Z. Liu, C. M. Rouleau, B. G. Sumpter, M. F. Chisholm, W. Zhou, P. D. Rack, D. B. Geohegan and K. Xiao, *J. Am. Chem. Soc.*, 2017, **139**, 14090–14097.

18 L.-H. Zeng, D. Wu, S.-H. Lin, C. Xie, H.-Y. Yuan, W. Lu, S. P. Lau, Y. Chai, L.-B. Luo, Z.-J. Li and Y. H. Tsang, *Adv. Funct. Mater.*, 2019, **29**, 1806878.

19 J. Yu, X. Kuang, Y. Gao, Y. Wang, K. Chen, Z. Ding, J. Liu, C. Cong, J. He and Z. Liu, *Nano Lett.*, 2020, **20**, 1172–1182.

20 Q. Liang, Q. Wang, Q. Zhang, J. Wei, S. X. Lim, R. Zhu, J. Hu, W. Wei, C. Lee and C. Sow, *Adv. Mater.*, 2019, **31**, 1807609.

21 M. Long, Y. Wang, P. Wang, X. Zhou, H. Xia, C. Luo, S. Huang, G. Zhang, H. Yan, Z. Fan, X. Wu, X. Chen, W. Lu and W. Hu, *ACS Nano*, 2019, **13**, 2511–2519.

22 J. Zhong, J. Yu, L. Cao, C. Zeng, J. Ding, C. Cong, Z. Liu and Y. Liu, *Nano Res.*, 2020, **13**, 1780–1786.

23 W. Xu, J. Jiang, H. Ma, Z. Zhang, J. Li, B. Zhao, R. Wu, X. Yang, H. Zhang, B. Li, W. Shu, Z. Zhang, B. Li, Y. Liu, L. Liao and X. Duan, *Nano Res.*, 2020, **13**, 2091–2097.

24 D. Wu, J. Guo, J. Du, C. Xia, L. Zeng, Y. Tian, Z. Shi, Y. Tian, X. J. Li, Y. H. Tsang and J. Jie, *ACS Nano*, 2019, **13**, 9907–9917.

25 A. M. Afzal, G. Dastgeer, M. Z. Iqbal, P. Gautam and M. M. Faisal, *ACS Appl. Mater. Interfaces*, 2020, **12**, 19625–19634.

26 D. Wu, C. Jia, F. Shi, L. Zeng, P. Lin, L. Dong, Z. Shi, Y. Tian, X. Li and J. Jie, *J. Mater. Chem. A*, 2020, **8**, 3632–3642.

27 Y. Ma, S. Zhang, S. Ding, X. Liu, X. Yu, F. Peng and Q. Zhang, *Opt. Laser Technol.*, 2020, **124**, 105959.

28 L. H. Zeng, Q. M. Chen, Z. X. Zhang, D. Wu, H. Yuan, Y. Y. Li, W. Qarony, S. P. Lau, L. B. Luo and Y. H. Tsang, *Adv. Sci.*, 2019, **6**, 1901134.

29 D. Li, J. Fu, P. Suo, W. Zhang, B. Lu, X. Lin, X. Yan, B. Li, G. Ma and J. Yao, *Appl. Phys. Lett.*, 2021, **118**, 191105.

30 T. V. Alencar, M. G. Silva, L. M. Malard and A. M. de Paula, *Nano Lett.*, 2014, **14**, 5621–5624.

31 H. Wang, C. Zhang and F. Rana, *Nano Lett.*, 2015, **15**, 339–345.

32 C. Soulard, X. Rocquefelte, P. E. Petit, M. Evain, S. Jobic, J. P. Itié, P. Munsch, H. J. Koo and M. H. Whangbo, *Inorg. Chem.*, 2004, **43**, 1943–1949.

33 J. Lin, S. Zuluaga, P. Yu, Z. Liu, S. T. Pantelides and K. Suenaga, *Phys. Rev. Lett.*, 2017, **119**, 016101.

34 A. P. Alexander, D. O. Akinola, X. Kai, V. H. Amanda, G. S. Bobby, M. David, B. G. David and L. Liangbo, *2D Mater.*, 2018, **5**, 035016.

35 J. Tauc, R. Grigorovici and A. Vancu, *Phys. Status Solidi B*, 1966, **15**, 627–637.

36 G. Zhang, M. Amani, A. Chaturvedi, C. Tan, J. Bullock, X. Song, H. Kim, D.-H. Lien, M. C. Scott and H. Zhang, *Appl. Phys. Lett.*, 2019, **114**, 253102.

37 A. P. Alexander, D. O. Akinola, X. Kai, V. H. Amanda, G. S. Bobby, M. David, B. G. David and L. Liangbo, *2D Mater.*, 2018, **5**, 035016.

38 A. Yamamoto, T. Mishina, Y. Masumoto and M. Nakayama, *Phys. Rev. Lett.*, 1994, **73**, 740–743.

39 J. Miller, J. Qi, Y. Xu, Y.-J. Cho, X. Liu, J. Furdyna, I. Perakis, T. Shahbazyan and N. Tolk, *Phys. Rev. B: Condens. Matter Mater. Phys.*, 2006, **74**, 113313.

40 Y. Xu, J. Qi, J. Miller, Y. J. Cho, X. Liu, J. Furdyna, T. Shahbazyan and N. Tolk, *Phys. Status Solidi C*, 2008, **5**, 2632–2636.

41 S. Ge, X. Liu, X. Qiao, Q. Wang, Z. Xu, J. Qiu, P. H. Tan, J. Zhao and D. Sun, *Sci. Rep.*, 2014, **4**, 5722.

42 X. Zhao, F. Liu, D. Liu, X.-Q. Yan, C. Huo, W. Hui, J. Xie, Q. Ye, C. Guo and Y. Yao, *Appl. Phys. Lett.*, 2019, **115**, 263102.

43 Q. Cui, F. Ceballos, N. Kumar and H. Zhao, *ACS Nano*, 2014, **8**, 2970–2976.

44 S. Meng, H. Shi, H. Jiang, X. Sun and B. Gao, *J. Phys. Chem. C*, 2019, **123**, 20051–20058.

45 L. Pi, C. Hu, W. Shen, L. Li, P. Luo, X. Hu, P. Chen, D. Li, Z. Li and X. Zhou, *Adv. Funct. Mater.*, 2021, **31**, 2006774.

46 X. Chen, S. Zhang, L. Wang, Y.-F. Huang, H. Liu, J. Huang, N. Dong, W. Liu, I. M. Kislyakov and J. M. Nunzi, *Photonics Res.*, 2019, **7**, 1416–1424.

47 C.-K. Sun, Y.-K. Huang, J.-C. Liang, A. Abare and S. P. DenBaars, *Appl. Phys. Lett.*, 2001, **78**, 1201–1203.

48 D. Lim, R. D. Averitt, J. Demsar, A. J. Taylor, N. Hur and S. W. Cheong, *Appl. Phys. Lett.*, 2003, **83**, 4800–4802.

49 P. Ruello and V. E. Gusev, *Ultrasonics*, 2015, **56**, 21–35.

50 Y. Xu, J. Qi, J. Miller, Y. J. Cho, X. Liu, J. K. Furdyna, T. V. Shahbazyan and N. Tolk, *Phys. Status Solidi C*, 2008, **5**, 2632–2636.

51 P. Soubelet, A. A. Reynoso, A. Fainstein, K. Nogajewski, M. Potemski, C. Faugeras and A. E. Bruchhausen, *Nanoscale*, 2019, **11**, 10446–10453.

52 C. Thomsen, J. Strait, Z. Vardeny, H. J. Maris, J. Tauc and J. Hauser, *Phys. Rev. Lett.*, 1984, **53**, 989.

53 Z. Huang, W. Zhang and W. Zhang, *Materials*, 2016, **9**, 716.

20674 | *Phys. Chem. Chem. Phys.*, 2021, **23**, 20666–20674

This journal is © the Owner Societies 2021